

A Wavelet-Based Electrogram Onset Delineator for Automatic Ventricular Activation Mapping

Alejandro Alcaine*, David Soto-Iglesias, Mireia Calvo, Esther Guiu, David Andreu, Juan Fernández-Armenta, Antonio Berruezo, Pablo Laguna, *Senior Member, IEEE*, Oscar Camara, and Juan Pablo Martínez

I. INTRODUCTION

Abstract—Electroanatomical mapping (EAM) systems are commonly used in clinical practice for guiding catheter ablation treatments of common arrhythmias. In focal tachycardias, the ablation target is defined by locating the earliest activation area determined by the joint analysis of electrogram (EGM) signals at different sites. However, this is currently a manual time-consuming and experience-dependent task performed during the intervention and thus prone to stress-related errors. In this paper, we present an automatic delineation strategy that combines electrocardiogram (ECG) information with the wavelet decomposition of the EGM signal envelope to identify the onset of each EGM signal for activation mapping. Fourteen electroanatomical maps corresponding to ten patients suffering from non-tolerated premature ventricular contraction (PVC) beats and admitted for ablation procedure were used for evaluation. We compared the results obtained automatically with two types of manual annotations: one during the intervention by an expert technician (on-procedure) and other after the intervention (off-procedure), free from time and procedural constraints, by two other technicians. The automatic annotations show a significant correlation (0.95, $p < 0.01$) with the evaluation reference (off-procedure annotation sets combination) and has an error of 2.1 ± 10.9 ms, around the order of magnitude of the on-procedure annotations error (-2.6 ± 6.8 ms). The results suggest that the proposed methodology could be incorporated into EAM systems to considerably reduce processing time during ablation interventions.

Index Terms—Activation mapping, bipolar electrogram, catheter ablation, electrophysiology, focal ventricular tachycardia, local activation time, signal envelope, wavelet analysis.

Manuscript received March 10, 2014; revised May 9, 2014; accepted June 4, 2014. Date of publication June 13, 2014; date of current version November 18, 2014. This work was supported by a personal grant to A.A. ref: BES-2011-046644, by projects TEC2010-21703-C03-02, TEC2013-42140-R, and TIN2011-28067 from Ministerio de Economía y Competitividad, and also by Aragón Government (Spain) and European Social Fund (EU) through Grupo Consolidado BSICoS and by CIBER de Bioingeniería, Biomateriales y Nanomedicina through Instituto de Salud Carlos III. *Asterisk indicates corresponding author.*

*A. Alcaine is with the BSICoS Group, Aragón Institute of Engineering Research (I3A), IIS Aragón, Universidad de Zaragoza, 50018 Zaragoza, Spain, and is also with the Centro de Investigación Biomédica en Red de Bioingeniería, Biomateriales y Nanomedicina (CIBER-BBN), 28029 Madrid, Spain (e-mail: aalcaineo@unizar.es).

D. Soto-Iglesias and O. Camara are with the PhySense Group, Department of Information and Communication Technologies, Universitat Pompeu Fabra, 08018 Barcelona, Spain (e-mail: david.soto@upf.edu; oscar.camara@upf.edu).

M. Calvo, E. Guiu, D. Andreu, J. Fernández-Armenta, and A. Berruezo are with the Arrhythmia Section, Cardiology Department, Thorax Institute, Hospital Clínic, Universitat de Barcelona, 08036 Barcelona, Spain (e-mail: calvo@clinic.ub.es; esguiu@clinic.ub.es; dandreu@clinic.ub.es; jufernan@clinic.ub.es; berruezo@clinic.ub.es).

P. Laguna and J. P. Martínez are with the BSICoS Group, Aragón Institute of Engineering Research (I3A), IIS Aragón, Universidad de Zaragoza, 50018 Zaragoza, Spain, and also with the Centro de Investigación Biomédica en Red de Bioingeniería, Biomateriales y Nanomedicina (CIBER-BBN), 28029 Madrid, Spain (e-mail: laguna@unizar.es; jpmart@unizar.es).

Color versions of one or more of the figures in this paper are available online at <http://ieeexplore.ieee.org>.

Digital Object Identifier 10.1109/TBME.2014.2330847

CATHETER ablation is the recommended treatment for patients with or without structural heart disease who suffer from ventricular tachycardia (VT) in which antiarrhythmic drug therapy is ineffective [1]. Mechanisms underlying focal VTs are related with trigger activity, automatisms [2], [3], and microentry [1], [4]. Focal VTs are candidates for radiofrequency ablation treatment since ablating targets determined by the location of the earliest activation area often terminates the arrhythmia [1], [5], [6].

Activation mapping is commonly used to determine the earliest activation area in focal arrhythmias [5], [7], and has been proved to be more accurate in focus localization than other mapping strategies [8]. The aim of activation mapping is to create a representation of the excitation sequence of the heart. To do so, an EAM system is commonly used. It allows to have the 3-D location of the ablation catheter within the patient's heart displaying the electrical EGM characteristics as well as minimizing the fluoroscopy exposition of the patient and clinical staff [1].

The local activation time (LAT) is defined as the time when the catheter electrodes sense an activation wavefront with respect to a stable time point [1], [5] and it is typically used for activation mapping. Different LAT definitions are found in the literature according to the EGM signal acquisition, i.e., unipolar or bipolar EGMs. In unipolar EGMs, the maximum negative slope of the signal coincides with the upstroke of the cardiac action potential and therefore, with the true activation time [9], [10]. However, unipolar EGMs are not so commonly used in the clinical practice because they are prone to be disrupted by baseline wander, far field, and other electrical sources. Common LAT surrogates in bipolar EGM signals are 1) the maximal peak of the signal, 2) the maximal slope, and 3) the EGM activation onset, usually considered as the time instant when the potential changes more than 45° from the isoelectric line at recording paper speed of 100 mm/s [10]. However, there is not an established consensus on these surrogates. The first two cannot be reliably estimated when fractionated potentials are present [1] and the definition of the EGM onset is ambiguous since it depends on the used amplitude scale. Nevertheless, the EGM onset is a better marker for activation mapping than the maximal peak and slope estimates [11].

For activation mapping, EAM system software generally locates by default the single maximal peak of the bipolar EGM activation in a given window of interest. In order to perform activation mapping based on EGM onsets, EAM system operators need to manually identify it for each EGM signal [12],

which can easily be available in more than 100 different mapping points. This process becomes a very time-consuming task that may compromise the accuracy of the mapping procedure due to the stressing conditions during the intervention. Once this procedure is achieved for all the acquired mapping points, it is straightforward to identify the earliest activation area that will guide the ablation procedure using a color-coded scale of the activation pattern.

On the other hand, noninvasive imaging techniques to obtain the activation sequence in the heart have been recently shown to be a promising tool for planning ablation procedures by solving the inverse problem using body surface potential mapping. Currently, this is under investigation in animals and simulation models [13], [14].

Automatic analysis of EGM signals can significantly reduce intervention times and increase the robustness of the mapping procedure. In continuous recordings, some techniques have been used for activation cycle length detection and analysis [15]–[19], frequency analysis and organization [20], [21], cross-correlation measurements [22], activation morphology analysis [23], and nonlinear analysis [24]. Most of these techniques have been applied for atrial fibrillation analysis and characterization. In recordings using EAM systems, dominant frequency is typically used to guide the ablation procedure [25], [26].

Detection and delineation of the surface ECG signals are well-known tasks and numerous approaches for it can be found in the literature [27]. Nevertheless, this task is more challenging in the case of EGM signals due to the noisy and variable nature of the data and only a few approaches can be found in the literature. Oesterlein *et al.* [28] proposed the nonlinear energy operator for LAT computation but was only applied in simulated data. El Haddad *et al.* [29] also proposed an algorithm focused on detecting the onset and end of electrograms for atrial tachycardias.

In this paper, we present an automatic delineation strategy that combines information from the surface ECG with the wavelet decomposition of the EGM activation envelope in order to delineate the onset of the EGM activation, therefore obtaining fast and observer-independent activation maps for guiding the ablation treatment of focal VTs. The proposed method is evaluated in fourteen electroanatomical maps from ten patients undergoing catheter ablation due to non-tolerated PVC beats. For each map, two types of manual annotations are available, one obtained during the intervention and other obtained after the intervention by two other experts. Some preliminary results were already presented in [30].

This paper is organized as follows. In Section II, we present the clinical data used in this paper, the signal characteristics, and the validation data. The methods for delineation of the EGM onset and the evaluation protocol are described in Section III. In Section IV, we present the results. Discussion and conclusions are given in Sections V and VI, respectively.

II. MATERIALS

The clinical database used in this study is composed of ten patients suffering from non-tolerated PVC beats who were

admitted for ablation treatment at Hospital Clínic de Barcelona (Barcelona, Spain) and signed their informed consent. Fourteen electroanatomical maps were studied (ten right ventricle maps, four left ventricle maps). Each map was acquired using the CARTO 3 system (*Biosense Webster, Inc., Diamond Bar, CA, USA*). It uses low-power electromagnetic fields from three coils located in the back of the patient in order to triangulate the position of the catheter within the heart and display it in a computer screen [31].

For each patient, different number of mapping points were acquired, large enough to have sufficient anatomical and electrical information to support the clinical decision. The EGM onsets were manually obtained by the operator during the intervention in order to generate activation maps based on LATs and to identify the early activation area defining the ablation target. The total number of studied mapping points was 2138 (153 ± 67 points per map). Each point included 12-lead ECG signals and bipolar EGM signals from a 4-pole NaviStar Thermocool irrigated tip catheter (*Biosense Webster, Inc., Diamond Bar, CA, USA*). For mapping and ablation purposes, the distal EGM signal from the catheter was used. Those signals were acquired in a stepwise fashion with 1 kHz sampling frequency during 2.5 s assuring that the contact of the catheter tip was stable with the myocardial wall and having at least one PVC beat in the recording excerpt. The CARTO system stores the signal within a window spanning 2 s before and 0.5 s after the fiducial point of the PVC beat of interest. Bipolar EGM signals were band-pass filtered between 16 and 500 Hz with a 50 Hz power-line suppression notch filter.

In addition to the manual annotations obtained during the procedure (referred to in this paper as “*on-procedure*” annotations), a second type of annotations from two other expert technicians (blinded to the initial on-procedure annotation) were obtained after the intervention (referred to in this paper as “*off-procedure*” annotations). For each point, the technician annotated the EGM activation onset as the start of the first steep deflection. The LAT is then defined as the difference between the EGM activation onset and the fiducial point of the QRS complex.

III. METHODS

A. EGM Preprocessing: Signal Envelope

During arrhythmias, a large variety of activation morphologies could be present in EGM signals with different causes such as the passing of different activation wavefronts through the catheter sensors, wavefront collisions, blocked or slow conductions, the relative position between the activation focus and the electrodes or the contact of the electrode with the cardiac tissue [32], [33]. Thus, in order to minimize the influence of EGM morphological variations in detection performance, an envelope-based preprocessing step is proposed.

Let an EGM activation $x[n]$ be modeled as a positive valued low-pass signal $e[n]$ modulated by a cosine with modulation frequency ω_m and phase angle ϕ

$$x[n] = e[n] \cdot \cos(\omega_m n + \phi). \quad (1)$$

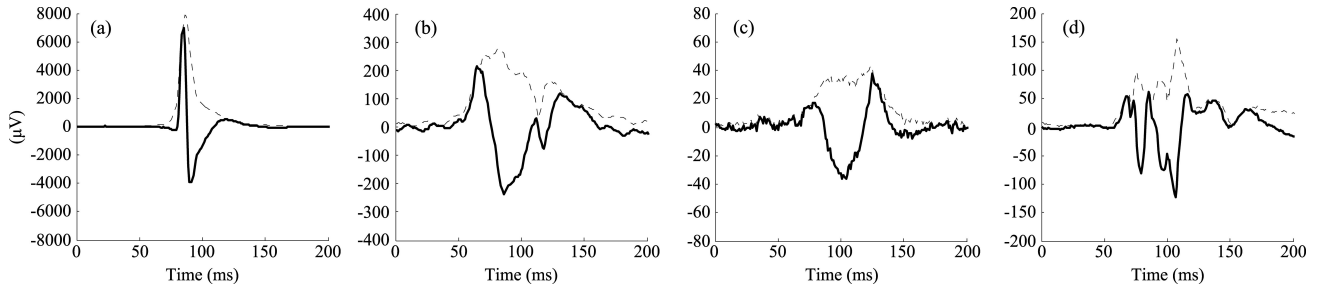


Fig. 1. EGM activations (bold line) and its envelope computation (dashed line): (a) Normal EGM activation, (b) noisy wide EGM activation, (c) low amplitude EGM activation, and (d) fractionated EGM activation.

The envelope $e[n]$ can be extracted by means of the analytic signal of $x[n]$ defined as in [34]

$$x_a[n] = x[n] + j\check{x}[n] \quad (2)$$

where j is the imaginary unit and $\check{x}[n]$ stands for the Hilbert transform of the signal $x[n]$, defined by

$$\check{x}[n] = \mathcal{H}\{x[n]\} = \frac{1}{\pi} \sum_{k=-\infty}^{\infty} \frac{x[k]}{n-k} \quad (3)$$

which is the convolution of $x[n]$ with an impulse response $h[n] = 1/\pi n$, known as the Hilbert transformer, whose transfer function is

$$H(e^{j\omega}) = \begin{cases} j, & -\pi \leq \omega < 0 \\ -j, & 0 \leq \omega < \pi \end{cases} \quad (4)$$

thus $\check{x}[n]$ is a 90° phase-shifted version of $x[n]$. Therefore, the analytic signal $x_a[n]$ represents a frequency-shifted version of the envelope $e[n]$

$$x_a[n] = e[n] \cdot e^{j\omega_m n} \quad (5)$$

from which the envelope $e[n]$ can be directly obtained, without any previous knowledge of the modulation frequency ω_m or phase angle ϕ , by means of the modulus

$$e[n] = |x_a[n]| = \sqrt{x^2[n] + \check{x}^2[n]}. \quad (6)$$

Fig. 1 shows representative examples of different EGM morphologies from the processed data and the computation of its envelope. It is noteworthy the heterogeneity of activation morphologies and amplitude levels that can be found in EGM signals.

B. Wavelet Transform

The continuous wavelet transform (CWT) is the decomposition of a given signal $x(t)$ into a set of basis functions created by dilation and translation of a single prototype function $\psi(t)$ called mother wavelet [35]. The CWT can be written as

$$W_a x(b) = \frac{1}{\sqrt{a}} \int_{-\infty}^{+\infty} x(t) \psi\left(\frac{t-b}{a}\right) dt, a > 0 \quad (7)$$

where a is the expansion factor and b is the translation factor. The CWT can be interpreted as the filtering of $x(t)$ with an

impulse response $h(t) = \psi(-t/a)/\sqrt{a}$. The expansion factor a modifies the bandwidth of the signal representation in the CWT domain, i.e., the larger is a , the wider is $\psi(t/a)$, and more information about lower frequencies is included in the CWT signal representation and vice versa.

If the prototype wavelet $\psi(t)$ is the derivative of a smoothing function $\theta(t)$, then (7) can be written as [36]

$$W_a x(b) = -a \left(\frac{d}{db}\right) \int_{-\infty}^{+\infty} x(t) \theta_a(t-b) dt \quad (8)$$

where $\theta_a(t) = (1/\sqrt{a})\theta(t/a)$ is the scaled version of the smoothing function. Therefore, the CWT at scale a is proportional to the derivative of the convolution of $x(t)$ with a smoothing impulse response at scale a . Then, the zero-crossings of the CWT correspond to local maxima or minima of the smoothed signal at different scales, and maximum or minimum values in the CWT are respectively associated with maximum upward or downward slopes in the smoothed signal.

Regarding our application, we are interested in locating the EGM activation onset in order to automatically compute LATs for activation maps. Therefore, these properties of the CWT combined with the positive valued low-pass EGM activation envelope $e[n]$ allow to have a representation of signal peaks as zero-crossings and its upward and downward slopes as maximum or minimum values in the CWT domain.

Given that the CWT is highly redundant, for implementation purposes, we consider a discrete signal $e[n]$ and discretize the CWT by means of the “dyadic discrete wavelet transform” (DWT). This consists of discretizing the time-scale plane parameters a and b following a dyadic sampling grid ($a = 2^m, b = 2^m l; m \in \mathbb{N}, l \in \mathbb{Z}$). Mallat and Zhong [36] demonstrates that the DWT is equivalent to an octave filter-bank that can be implemented as a cascade of identical cells of low-pass and high-pass finite impulse response (FIR) filters followed by decimation stages. We used the *algorithme à trous* for removing those decimation stages, keeping the time-invariance representation of the signal and the temporal resolution of the different scales while preserving the sampling rate [37]. The implemented analysis filter-bank of the Mallat’s algorithm using the *algorithme à trous* is shown in Fig. 2.

We used the derivative of a quadratic spline as prototype wavelet $\psi(t)$ that was already proposed for QRS detection and

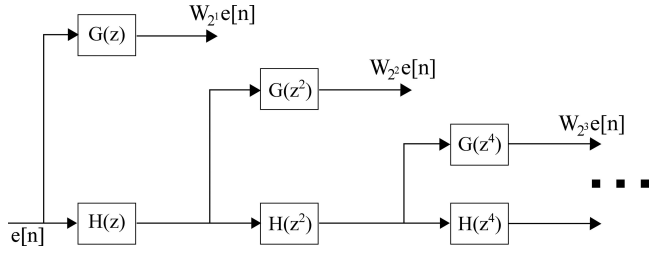


Fig. 2. Mallat's algorithm filter-bank implementation without decimation stages (*algorithme à trous*) where $G(z)$ and $H(z)$ are low-pass and high-pass FIR filters, respectively.

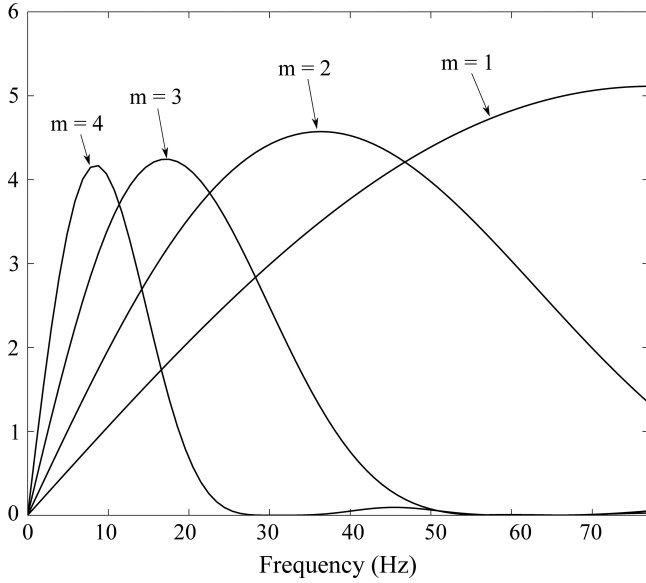


Fig. 3. Equivalent frequency responses of the DWT at scales 2^m , $m = 1 \dots 4$ for 1 kHz interpolation sampling frequency.

delineation in ECG signals [27] and atrial fibrillation cycle length analysis [19]. Using the *algorithme à trous* with this prototype wavelet, the transfer function of the first four scales for an interpolation sampling frequency of 1 kHz are shown in Fig. 3. These transfer functions behave as low-pass differentiator filters with linear phase [27]. Hence, the wavelet-based activation onset delineator presented in this paper can be considered as a low-pass differentiator filter-bank.

C. Description of the Detection Algorithm

The algorithm presented in this paper is based in the outcomes of a two-step signal analysis strategy, as illustrated in Fig. 4.

1) *QRS Delineation of the Reference Beat*: The main goal of this detection step is to characterize the beat of interest and then provide a reference window for the EGM delineation algorithm. A single-lead wavelet-based QRS detector and delineator were applied on each surface ECG lead [27]. This process identify three time instants for each lead l and beat i within the recording excerpt: 1) the onset of the i th QRS complex $n_o^{l,i}$, 2) the fiducial point of the i th QRS complex $n_f^{l,i}$ (usually related with the R wave), and 3) the end of the i th QRS complex $n_e^{l,i}$.

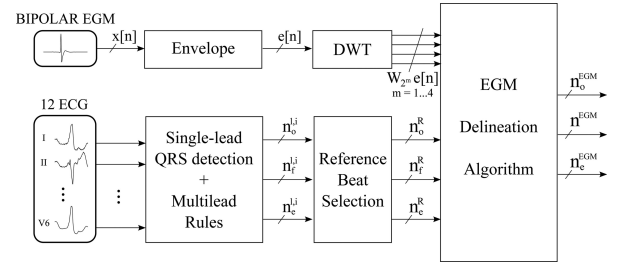


Fig. 4. Block diagram of the signal analysis strategy. The EGM delineation algorithm uses the DWT of the bipolar EGM activation envelope (top branch) aided by the QRS delineation of the reference beat (bottom branch).

In this step, we are mainly interested in obtaining a global view of each beat. Therefore, a multilead delineation is performed using the rule algorithm described in [38]. These rules were designed to include the spatiotemporal information of each ECG lead while avoiding errors and miss-detections, obtaining temporal marks that were in agreement across the different leads of the recording.

After obtaining the multilead delineation, the nearest QRS fiducial point to the reference time (2000 ms) defines the reference beat fiducial point n_f^R . This point and its related onset and end time instants (n_o^R and n_e^R) describe the reference beat. The onset and end time points of the reference QRS beat are used to define the basic searching window S (marked as blue dotted vertical lines in each panel of Fig. 5).

2) *EGM Delineation Algorithm*: After QRS detection and delineation of the reference beat, an EGM delineation strategy is applied to the DWT of the bipolar EGM signal envelope.

The strategy presented here is inspired on the multiscale approach used in [27], whose objective is to locate a set of local maxima and minima across the different scales of the DWT, called “*Maximum Modulus Lines*” (MML) [39]. The first step of the algorithm is to locate the highest peak of the EGM signal envelope that define the “*activation main wave*”. Since the EGM activation envelope is a positive peaked signal, the activation main wave is related with the zero-crossings between a pair of positive and negative MMLs in the DWT domain. A local maximum or minimum value at scale 2^m can be considered a part of a MMLs if it is higher than a threshold defined as

$$\varepsilon_{\text{EGM}}^m = \epsilon_m \sqrt{\frac{1}{L} \sum_{n \in S} (W_{2^m} e[n])^2}, \quad m = 1 \dots 4 \quad (9)$$

where $\epsilon_4 = 3/4$ and $\epsilon_m = 3/8$, $m = 1 \dots 3$ are the threshold scaling factors of each scale and L stands for the length of the window S . Given the frequency content of the EGM envelope, their frequency components are more likely to lie at scales 2^4 and 2^3 (see Fig. 3).

In this paper, we were mainly interested in locating EGM activations during PVCs, and these can occur outside the QRS complex boundaries of the reference beat. Therefore, S is extended in both ends by 30 ms defining the extended window S' . Within S' , those local maxima and minima values exceeding at scale 2^4 the threshold $\varepsilon_{\text{EGM}}^4$ defined by (9) were detected.

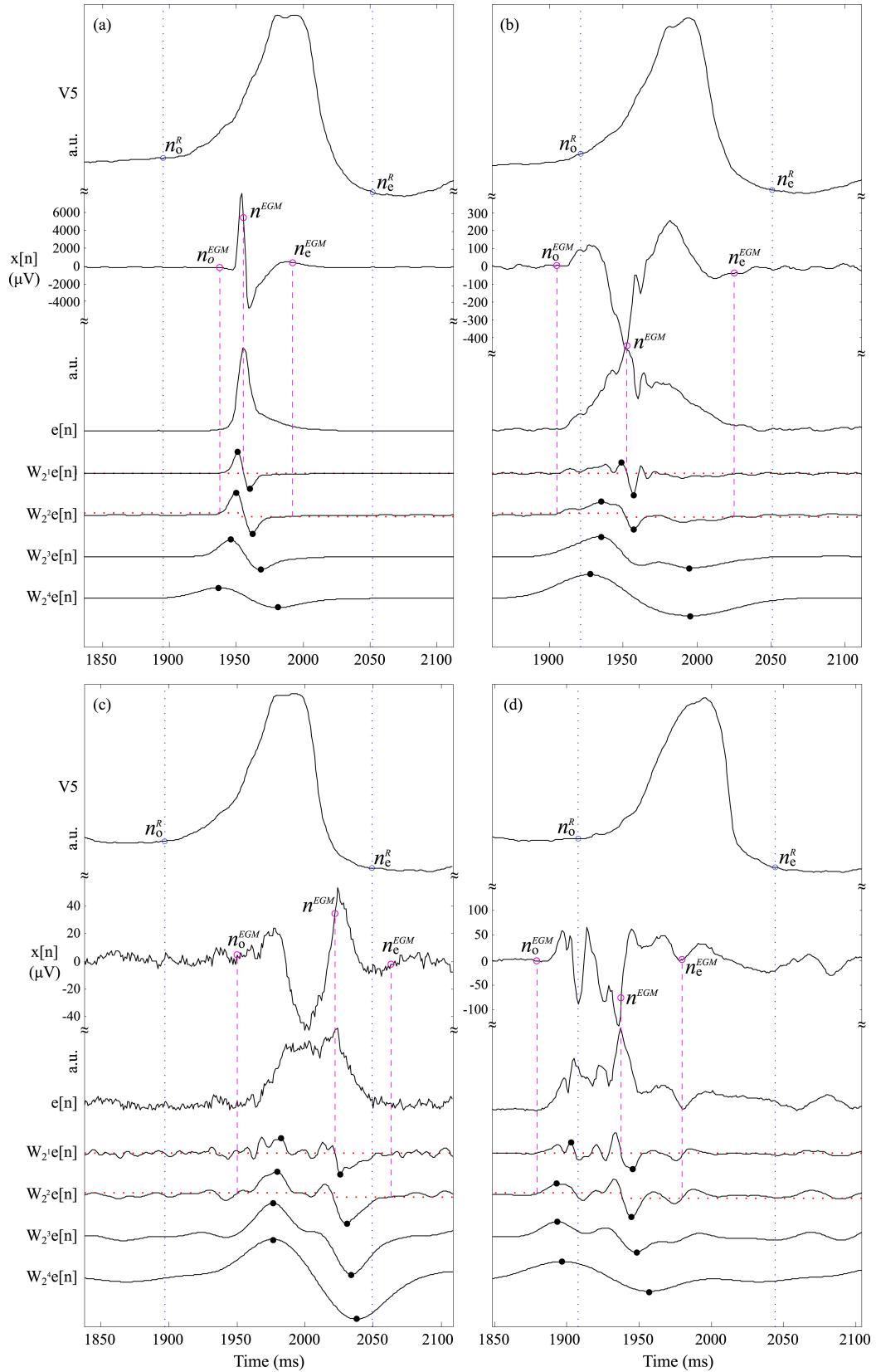


Fig. 5. Automatic detection results in four representative EGM activation shapes: (a) Normal EGM activation, (b) noisy wide EGM activation, (c) low amplitude EGM activation, and (d) fractionated EGM activation. Each panel shows, centered at the reference beat and from top to bottom: V5 surface ECG lead, distal EGM lead from mapping catheter $x[n]$, its envelope $e[n]$ and the four first scales of the wavelet transform $W_{2^m} e[n]$, $m = 1 \dots 4$ with the detected MMLs marked in black dots. Blue dotted vertical lines shows the estimated QRS complex width (from n_o^R to n_c^R) which serves as the search window S . Purple dashed vertical lines connect the DWT characteristic landmarks (each one obtained from the crossing with the red dotted horizontal lines that represent for scale 2^1 the zero level and for scale 2^2 thresholds ξ_o^{EGM} and ξ_c^{EGM}) with their resulting annotations: the main wave n^{EGM} and its onset and end points n_o^{EGM} and n_c^{EGM} , respectively.

If the extended search window was inadequate for finding at least a pair of local maximum–minimum (LMM) at scale 2^4 , a new searching procedure was performed by extending 30 ms S' , forward or backward depending on the sign of the already detected local maxima and minima, and applying a threshold reduction by 50% of the previous value. If there was no success in the LMMs searching procedure at scale 2^4 , then scale 2^3 was used for LMM detection in combination with the threshold $\varepsilon_{\text{EGM}}^3$ defined by (9). This scale includes higher frequency components of the signal than scale 2^4 but it is usually noisier.

Once LMM pairs were located at the appropriate detection scale (either 2^4 or 2^3), MML searching across the rest of the scales was performed by connecting the local maxima and minima detected using their corresponding thresholds defined by (9), followed by rejection of those isolated and redundant lines in the same way as in [27].

When a single zero-crossing between a pair of positive and negative MMLs at scale 2^1 is present, it is marked as the main activation wave n^{EGM} as shown in the two upper panels of Fig. 5. In case that more than one zero-crossings exist between a pair of positive and negative MMLs at scale 2^1 , the main wave n^{EGM} is determined by selecting among the possible pairs of LMM candidates, the zero-crossing at scale 2^1 whose associated LMM pair presents higher maximum-to-minimum value. The result of this procedure can be seen in the two lower panels of Fig. 5.

Once the activation main wave is detected, the next step of the algorithm is to delineate the onset and end points of the current EGM activation. The algorithm starts from the formerly detected n^{EGM} , which will be flanked by a pair of positive and negative MMLs at scale 2^2 . Local maximum or minimum values at scale 2^2 are related to up and down slopes of the EGM signal envelope, respectively. Therefore, the EGM activation onset point n_o^{EGM} is detected as the single first sample below a threshold defined as

$$\xi_o^{\text{EGM}} = \gamma_o \cdot \max(W_{2^2} e[n]), n \in S_o \quad (10)$$

where $\gamma_o = 0.1$ is the proportional threshold factor. This threshold is computed within a window S_o that spans 30 ms before n^{EGM} . An example of this delineation process is shown in Fig. 5(a). In order to protect the method against fractionated and noisy EGM activations, as those shown in Fig. 5(b)–(d), the algorithm only considers those candidate samples lying within the biggest upward slope at scale 2^4 . This scale is related with the overall shape of the EGM activation envelope. Detection of the EGM activation end point n_e^{EGM} is done using a similar but symmetric procedure.

D. Evaluation Protocol

In the absence of a systematic well-established rule for LAT measurement as “gold standard” for activation mapping, we considered the manual annotations performed after the intervention (off-procedure annotations) as the reference for evaluation. The difference between annotations performed during the procedure (on-procedure) with respect to the off-procedure

TABLE I
ERRORS COMPARED WITH THE AVERAGED OFF-PROCEDURE ANNOTATIONS SET INCLUDING THE INTEREXPERT DIFFERENCE (MEAN \pm SD) AND SPEARMAN’S RANK CORRELATION VALUE ρ_s

| Map (#) | Points (#) | Automatic (ms) | ρ_s | On-procedure (ms) | ρ_s | Difference (ms) | ρ_s |
|---------|------------|----------------|----------|-------------------|----------|-----------------|----------|
| 1 | 134 | 0.1 \pm 7.1 | 0.97* | -3.3 \pm 5.9 | 0.98* | -2.2 \pm 4.1 | 0.99* |
| 2 | 116 | 1.2 \pm 9 | 0.9* | -2.9 \pm 4.8 | 0.96* | -0.8 \pm 3.6 | 0.97* |
| 4 | 190 | 0.5 \pm 6.3 | 0.82* | -3.1 \pm 4.2 | 0.92* | -1.3 \pm 3.6 | 0.95* |
| 5 | 220 | 0.7 \pm 8.8 | 0.94* | -6.7 \pm 7.4 | 0.96* | -1.7 \pm 4.4 | 0.99* |
| 6 | 234 | 1.6 \pm 8.4 | 0.92* | 0.4 \pm 3.8 | 0.98* | -0.3 \pm 3.9 | 0.97* |
| 8 | 208 | 5 \pm 10.3 | 0.93* | -1.8 \pm 7 | 0.96* | -1.1 \pm 3.3 | 0.98* |
| 9 | 172 | 3.8 \pm 12.6 | 0.83* | -3.1 \pm 6.2 | 0.94* | -1.1 \pm 3.4 | 0.98* |
| 10 | 197 | 4.1 \pm 11.2 | 0.95* | -4.7 \pm 8.1 | 0.97* | -0.6 \pm 2.8 | 0.99* |
| 11 | 202 | 1.5 \pm 17.9 | 0.89* | 1.4 \pm 7.5 | 0.95* | 1.1 \pm 8.0 | 0.95* |
| Total | 1673 | 2.1 \pm 10.9 | 0.95* | -2.6 \pm 6.8 | 0.98* | -0.8 \pm 4.5 | 0.99* |

* Indicates a p -value < 0.01 .

annotations was considered as a reference for performance comparison.

Due to technician availability, only nine maps with annotations performed by both technicians were available. Therefore, in order to have more reliable annotations for performance evaluation, we computed the average value between both sets of annotations and create the “averaged off-procedure” annotation set which serves as evaluation reference. Additionally, we defined the set of annotations performed by a single technician named “off-procedure annotation set 1” (with fourteen maps annotated) and “off-procedure annotation set 2” (with nine maps annotated).

Errors between annotations were computed and mean \pm standard deviation (SD) were presented. Due to the ordered nature of LATs (i.e., from earliest to latest activated point) and in order to estimate the agreement in the sequences of activations obtained with the different LAT annotations, Spearman’s rank correlation ρ_s has been computed. Additionally, we use Lin’s concordance correlation factor ρ_c [40] and Bland–Altman analysis for assessing agreement between the different LAT annotations. A p -value ≤ 0.05 was considered as a threshold for statistical significance.

IV. RESULTS

A. Double Expert Assessment

The error of the proposed algorithm compared with the evaluation reference is shown in the third column of Table I. It is noteworthy to point out that the bias of the error is positive, thus meaning that the automatic method provides slightly later LATs than the reference. For comparison purposes, the error of the on-procedure annotations is shown in the fifth column of Table I. This error has a negative bias thus meaning that the on-procedure annotations provide slightly earlier LATs than the reference.

Spearman’s rank correlation value ρ_s is shown in columns four and six of Table I. The correlation of the automatic annotations with the evaluation reference is high ($\rho_s = 0.95$) but inferior than the on-procedure annotations ($\rho_s = 0.98$). Moreover, all correlation values are statistically significant ($p < 0.05$).

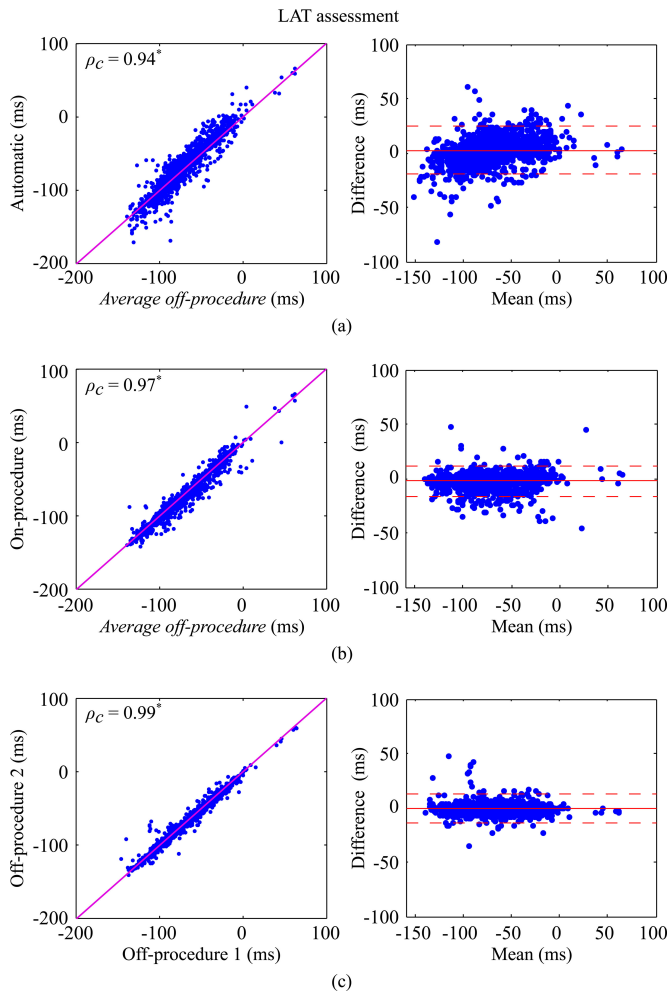


Fig. 6. Lin's concordance correlation factor ρ_c (left panels) and Bland–Altman plots (right panels) for: (a) LAT assessment of the automatic annotations with the “averaged off-procedure” annotations, (b) LAT assessment of the on-procedure annotations with the “averaged off-procedure” annotations, and (c) interexpert LAT assessment. Pink line indicates the unitary slope line for Lin's ρ_c assessment. *Indicates a p -value < 0.01 . Red continuum line indicates mean error/difference and red slashed lines indicates mean ± 2 SD of error/difference.

The difference between off-procedure annotation sets, i.e., the interexpert variability, is shown in columns seven and eight of Table I. The variability between experts can be considered as a lower bound for automatic and on-procedure annotations since a difference smaller than this could mean that the method over adapt to one of the experts. Spearman's correlation factor ρ_s shows a high correlation values ($\rho_s = 0.99$) indicating the high level of agreement between technicians in the same conditions.

Fig. 6 shows the Lin's concordance correlation factor ρ_c (left panels) and Bland–Altman plot analysis (right panels) for the error (panels of rows (a) and (b) of Fig. 6) and the interexpert variability (panels of row (c) of Fig. 6). Lin's ρ_c confirm the correlation found with Spearman's ρ_s . Bland–Altman plots also confirm the agreement found in Table I and show that the LATs computed with the presented algorithm has a slight linear tendency (Pearson's $\rho = 0.37$, $p < 0.01$) toward early estimation

TABLE II
CLASSIFICATION OF ANNOTATIONS ACCURACY COMPARED WITH THE AVERAGED OFF-PROCEDURE ANNOTATION SET

| | Automatic (%) | On-Procedure (%) |
|-----------------|---------------|------------------|
| Highly accurate | 51 | 74 |
| Accurate | 23 | 16 |
| Inaccurate | 26 | 10 |

of the early LATs with activation times from -150 to -50 ms from the QRS fiducial point.

Inspired by the accuracy evaluation proposed by El Haddad *et al.* [29], Table II shows the three-level accuracy distribution of the automatic and on-procedure annotations compared with the evaluation reference: 1) *highly accurate* annotations (error $\leq \pm 5$ ms), 2) *accurate* annotations (error within ± 5 ms and ± 10 ms), and 3) *inaccurate* annotations (error $> \pm 10$ ms). This table shows that the 74% of the mapping points annotation obtained with the automatic algorithm are considered as *accurate* or *highly accurate* compared with the evaluation reference. Nevertheless, the performance of the automatic detection is still inferior to the 90% of on-procedure mapping point annotations considered as *accurate* or *highly accurate* annotations.

These results demonstrate an agreement of the proposed method with the expert manual annotations that is acceptable for clinical application. Fig. 7 shows two representative examples of 3-D activation maps obtained with all the LAT annotation sets of this study. Those 3-D maps are generated by discretizing the colorscale into 10 ms isochrone areas (defined as those areas whose mapping point LATs lie within a temporal interval of 10 ms starting from the earliest activated EGM mapping point in 10 ms steps) as it is usually done in clinical practice [6]. The earliest activation area is located in the right ventricle outflow tract for all maps, since data are mainly coming from idiopathic cardiomyopathy patients. Moreover, in both examples, a concentric spreading of the activation is more clearly seen in the automatic reconstructed map, as it would be expected in case of focal activity [11]. The effective ablation point (pink spheres pointed by white arrows) lies within the two first isochrone areas in all cases. In those examples, errors of 3.8 ± 12.6 ms and 5 ± 10.3 ms for maps #9 and #8, respectively, do not result in a lack of precision in determining the earliest activation area for ablation of focal VTs.

B. Single Expert Assessment

As previously mentioned in Section III, the *off-procedure annotation set 1* has annotated all patients and maps of the study database. In order to evaluate the performance of the automatic method in all maps, we compute the error using this set as an additional reference. This error as well as the error of the on-procedure annotation are shown in Table III. It shows an increment of the error, especially in the case of the automatic annotations (2.2 ± 12.4 ms), as compared with results shown in Table I.

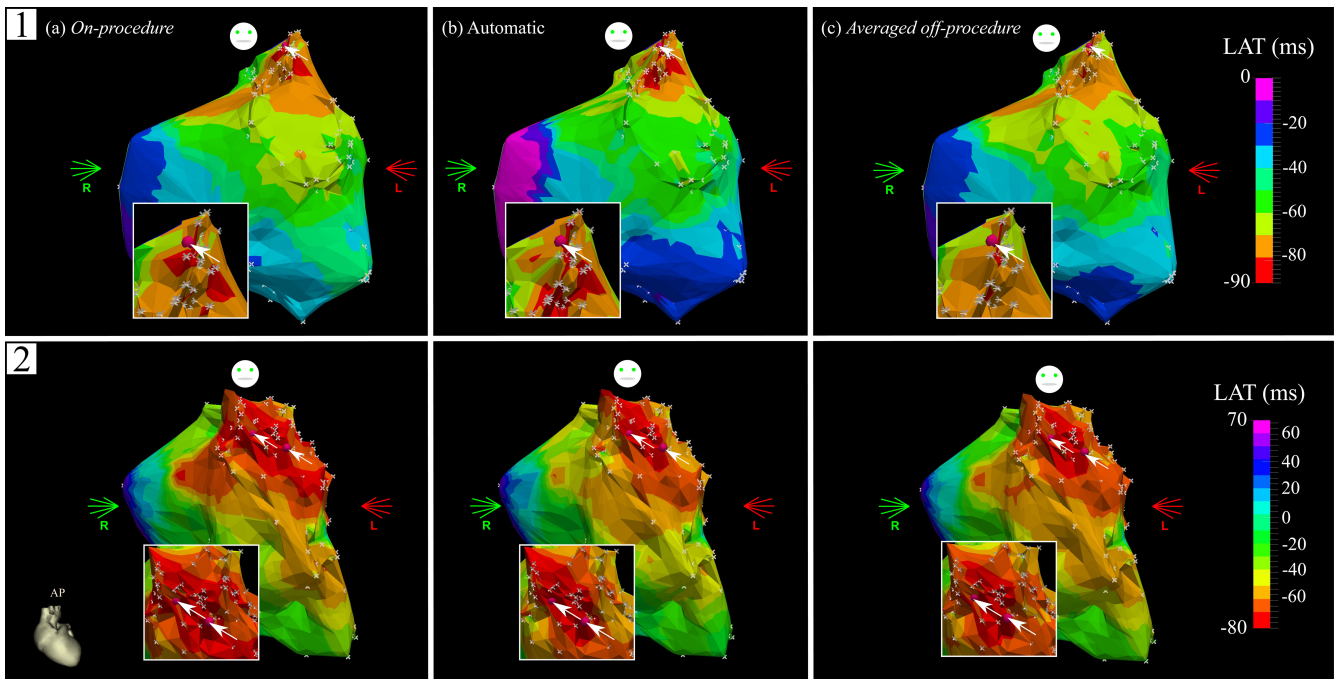


Fig. 7. Example of two activation map #9 (labeled as 1) and #8 (labeled as 2) corresponding to the right ventricle shown in anterior-posterior (AP) view including a zoom view (white square) of the earliest activation area: (a) LATs from the on-procedure annotation set, (b) obtained LATs with the automatic algorithm presented in this paper, and (c) using the “averaged off-procedure” LATs annotation considered as evaluation reference. LATs are shown in 10 ms isochrone areas color-coded from red (earlier) to pink (later) referenced to the QRS complex. White crosses indicate the acquired mapping points and pink spheres pointed by white arrows indicate the effective ablation point/s that terminated the arrhythmia.

TABLE III
ERRORS COMPARED WITH THE OFF-PROCEDURE ANNOTATION SET 1 (MEAN \pm SD) AND SPEARMAN’S RANK CORRELATION VALUE ρ_s .

| Map (#) | Points (#) | Automatic (ms) | ρ_s | On-Procedure (ms) | ρ_s |
|---------|------------|-----------------|------------------|-------------------|----------|
| 1 | 134 | -1.2 ± 7.9 | 0.96* | -4.6 ± 6.4 | 0.97* |
| 2 | 116 | 0.6 ± 9.4 | 0.9* | -3.5 ± 5.4 | 0.94* |
| 3 | 163 | 10.8 ± 11.8 | 0.9* | 3.3 ± 5 | 0.98* |
| 4 | 190 | -0.3 ± 6.6 | 0.82* | -4.0 ± 5.5 | 0.9* |
| 5 | 220 | -0.3 ± 9.4 | 0.94* | -7.8 ± 8 | 0.95* |
| 6 | 264 | 1.2 ± 8.8 | 0.91* | 0.2 ± 4.8 | 0.97* |
| 7 | 49 | 7.4 ± 14.1 | 0.68* | 0 ± 5.3 | 0.96* |
| 8 | 208 | 4.2 ± 10.7 | 0.92* | -2.6 ± 7.4 | 0.95* |
| 9 | 172 | 3.0 ± 13 | 0.82* | -3.9 ± 6.8 | 0.93* |
| 10 | 197 | -4.6 ± 7.7 | 0.95* | -5.3 ± 8.5 | 0.96* |
| 11 | 202 | 1.9 ± 18.7 | 0.86* | 1.7 ± 7.8 | 0.96* |
| 12 | 96 | 5.2 ± 17.3 | 0.68* | 3.4 ± 6.7 | 0.91* |
| 13 | 87 | -1.0 ± 12.4 | 0.59* | 2.1 ± 6.3 | 0.81* |
| 14 | 40 | -7.3 ± 20.7 | 0.4 [†] | 4.1 ± 5.4 | 0.93* |
| Total | 2138 | 2.2 ± 12.4 | 0.93* | -1.9 ± 7.5 | 0.97* |

* Indicates a p -value < 0.01 and [†] indicates a p -value < 0.05

C. Execution Time

A low-computational time of the algorithm is important for being included into an EAM system software and for its application in real time during clinical routine. The complete process of ECG and EGM detection and delineation is done in 760 ± 24 ms/mapping point with a regular computer (Windows 7 based PC, Intel Core i7 3.4 GHz, 8 Gb RAM with MATLAB R2010a) where only 14.7% of that time correspond to the EGM detection and delineation itself (112 ± 6 ms/mapping point).

V. DISCUSSION

There is no clear consensus regarding the measurement of LATs in bipolar EGMs [5], [10], especially when fractionated or split potentials are present [1]. However, detection of the earliest activation area by means of locating the onset of the bipolar EGM has been shown to be useful for the treatment of focal arrhythmias [5], [6]. In addition, some definitions of the activation onset [10] seem to be arbitrary as they depend on the amplitude scale of the activation. Hence, the identification of the activation onset for LAT computation in activation mapping is a strongly observer-dependent task that complicates the selection of a reliable reference annotations for evaluation.

EAM systems are useful tools for cardiac mapping as they allow to have a 3-D location of the mapping catheter within the patient’s heart combined with the electrical properties of the cardiac substrate [1]. However, they do not provide an automatic measurement of LATs using the EGM activation onset. Therefore, this must be made manually by the operator, turning into a highly time-consuming task.

In this paper, we have presented an automatic wavelet-based EGM delineation algorithm for activation mapping of focal VTs. The complete process is the combination of a two-step signal analysis. First, detection and delineation of the beat of interest in the surface ECG is performed. The second step uses this delineation as a basic window for the EGM delineation algorithm. The proposed algorithm exploits the DWT time-scale characteristics of the EGM activation envelope signal in order to identify the EGM activation onset providing an automatic activation mapping based on LATs. As a secondary

result, the end of the activation is delineated in a symmetric manner and can be a useful measurement in further studies. In addition, this algorithm uses the same filter-bank structure as the QRS detector, hence providing unified scheme and criteria.

Recently, an algorithmic detection of the onset and end of bipolar EGM signal based in a four-state machine was presented for atrial tachycardias [29]. This algorithm identifies the activation onset and end by counting the samples where a rectified band-pass filtered bipolar EGM activation is above or below a set of thresholds adapted to the studied database by trial-error process and its accuracy evaluation was done by visual inspection in a small set of electroanatomical mapping points from randomized patients. Due to the lack of standard databases with reference annotations by expert physicians and the different objectives of both methodologies, its comparison is rather difficult. Moreover, our method shows a simplest and direct relation between threshold factor γ_0 and annotation outcomes, making it more simple to adjust its performance. To our knowledge, this paper is the first work comparing automatic annotations with manual references of LAT based on EGM onsets obtained during and after the intervention by different experts.

Results suggest a good agreement between the proposed method with expert annotations for clinical purposes. The error compared with the combination of annotations from two experts (*average off-procedure* annotation set) is 2.1 ± 10.9 ms and correlation with the evaluation reference is high ($\rho_s = 0.95$). The error bias is positive, meaning that our method provides slightly later LATs than the reference. In terms of the accuracy of the annotations, 74% of the evaluated mapping points are considered as *accurate* or *highly accurate*. The error increases up to 2.2 ± 12.4 ms and the correlation decreases to $\rho_s = 0.93$ when only the annotation set from a single expert is considered as reference.

The automatic method does not perform better than the on-procedure annotations when compared with the evaluation reference (error of -2.6 ± 6.8 ms and $\rho_s = 0.98$). The negative error bias indicates that the on-procedure annotations provide slightly earlier LATs than the reference. Moreover, 90% of the evaluated mapping points are considered as *accurate* or *highly accurate* annotated. This better accuracy of the on-procedure annotations can be explained by the fact that the three technicians use the same software for manual annotations that displays in real time the activation map and signals, allowing to compare the current measured onsets with those already acquired points in the vicinity. This process allows the technicians to modify their decision in order to obtain a smoothed *spatially coherent* activation map, especially in the earliest activation area which usually has the higher concentration of mapping points. This is clearly an advantage with respect to the automatic method since, at the time being, it does not exploit the anatomy or location of the mapping points and its vicinity relations. Future work should be focused on adding spatially coherent constraints in the delineation algorithm.

In terms of computational cost, our algorithm detects the bipolar EGM activation onset in 112 ± 6 ms, a small percentage

of the total processing time per mapping point (760 ± 24 ms). It also should be noted that the computation time associated with the surface ECG delineation can be neglected in real applications since it can be performed online. Based on the experience of our technicians, the manual on-procedure annotations were performed within 3 to 4 s per point. Moreover, note that the larger part of the acquisition time is due to the necessary operations of the physician for positioning and stabilizing the catheter and the occurrence of a PVC beat during the intervention. Therefore, the computational time of the proposed signal processing method can be considered negligible.

Threshold factors and intervals shown in this paper were selected based on our electrophysiological background and technical experience with surface ECG detection and delineation, thus being a limitation of this study since we did not perform a sensitivity analysis of them. Therefore, further investigation of its influence and generalization to other datasets is needed.

VI. CONCLUSION

This paper presents an automatic wavelet-based strategy to identify EGM activation onset for activation mapping during focal VTs. If integrated with EAM systems, the proposed automatic method and its associated low computation costs could help physicians and technicians to reduce signal acquisition time and intervention since it is able to automatically identify the EGM activation onset in less than 1 s. This could eventually be more beneficial when applied on EAM data acquired with multielectrode catheters. These catheters are able to acquire multiple EGM signals at one single beat and thus generate high-density activation maps, making the creation of accurate activation maps based on LAT onsets unaffordable without automatic or semiautomatic signal processing techniques.

This paper is initially focused on focal VTs since more complex tachycardias, like those driven by conduction channels in big areas of myocardium scar, require more complex and adapted detection and characterization algorithms. Nevertheless, the presented algorithm can be a good starting point and will be specifically adapted for the detection of conduction channels on ischemic patients [41].

REFERENCES

- [1] E. M. Aliot, W. G. Stevenson, J. M. Almendral-Garrote, F. Bogun, C. H. Calkins, E. Delacretaz, P. D. Bella, G. Hindricks, P. Jaïs, M. E. Josephson, J. Kautzner, G. N. Kay, K.-H. Kuck, B. B. Lerman, F. Marchlinski, V. Reddy, M.-J. Schalij, R. Schilling, K. Soejima, and D. Wilber, "EHRA/HRS expert consensus on catheter ablation of ventricular arrhythmias: Developed in a partnership with the European Heart Rhythm Association (EHRA), a registered branch of the European Society of Cardiology (ESC), and the heart rhythm society (HRS); in collaboration with the American College of Cardiology (ACC) and the American Heart Association (AHA)," *Europace*, vol. 11, no. 6, pp. 771–817, 2009.
- [2] H. Tada, K. Tadokoro, S. Ito, S. Naito, T. Hashimoto, K. Kaseno, K. Miyaji, A. Sugiyasu, T. Tsuchiya, Y. Kutsumi, A. Nogami, S. Oshima, and K. Taniguchi, "Idiopathic ventricular arrhythmias originating from the tricuspid annulus: Prevalence, electrocardiographic characteristics, and results of radiofrequency catheter ablation," *Heart Rhythm*, vol. 4, no. 1, pp. 7–16, 2007.
- [3] B. B. Lerman, "Mechanism of outflow tract tachycardia," *Heart Rhythm*, vol. 4, no. 7, pp. 973–976, 2007.

- [4] B. Philips, S. Madhavan, C. James, C. Tichnell, B. Murray, M. Needleman, A. Bhonsale, S. Nazarian, K. R. Laurita, H. Calkins, and H. Tandri, "High prevalence of catecholamine-facilitated focal ventricular tachycardia in patients with arrhythmogenic right ventricular dysplasia/cardiomyopathy," *Circulation: Arrhythmia Electrophysiol.*, vol. 6, no. 1, pp. 160–166, 2013.
- [5] C. Weiss, S. Willems, R. Rueffel, M. Hoffmann, and T. Meinertz, "Electroanatomical mapping (CARTO[®]) of ectopic atrial tachycardia: impact of bipolar and unipolar local electrogram annotation for localization of the focal origin," *J. Int. Cardiac Electrophysiol.*, vol. 5, no. 1, pp. 101–107, 2001.
- [6] C. Herczku, A. Berruezo, D. Andreu, J. Fernández-Armenta, L. Mont, R. Borràs, E. Arbelo, J. M. Tolosana, E. Trucco, J. Ríos, and J. Brugada, "Mapping data predictors of a left ventricular outflow tract origin of idiopathic ventricular tachycardia with V3 transition and septal earliest activation," *Circulation: Arrhythmia Electrophysiol.*, vol. 5, no. 3, pp. 484–491, 2012.
- [7] R. John and W. Stevenson, "Catheter-based ablation for ventricular arrhythmias," *Current Cardiol. Rep.*, vol. 13, no. 5, pp. 399–406, 2011.
- [8] F. Morady, A. H. Kadish, L. Di Carlo, W. H. Kou, S. Winston, M. DeBuitier, H. Calkins, S. Rosenheck, and J. Sousa, "Long-term results of catheter ablation of idiopathic right ventricular tachycardia," *Circulation*, vol. 82, no. 6, pp. 2093–2099, 1990.
- [9] M. S. Spach, W. T. Miller, E. Miller-Jones, R. B. Warren, and R. C. Barr, "Extracellular potentials related to intracellular action potentials during impulse conduction in anisotropic canine cardiac muscle," *Circulation Res.*, vol. 45, no. 2, pp. 188–204, 1979.
- [10] T. Paul, J. P. Moak, C. Morris, and A. Garson, Jr., "Epicardial mapping: How to measure local activation?," *Pacing Clin. Electrophysiol.*, vol. 13, no. 3, pp. 285–292, 1990.
- [11] Z. Issa, J. M. Miller, and D. P. Zipes, *Clinical Arrhythmology and Electrophysiology: A Companion to Braunwald's Heart Disease*. 2nd ed. Philadelphia, PA, USA: Saunders, 2012.
- [12] J. M. Hsing, P. Zei, H. H. Hsia, P. J. Wang, and A. Al-Ahmad, *Cardiac Mapping*. 3rd ed. Hoboken, NJ, USA: Wiley, 2009, ch. 10.
- [13] C. Han, S. M. Pogwizd, C. R. Killingsworth, and B. He, "Noninvasive imaging of three-dimensional cardiac activation sequence during pacing and ventricular tachycardia," *Heart Rhythm*, vol. 8, no. 8, pp. 1266–1272, 2011.
- [14] C. Liu and B. He, "Noninvasive estimation of global activation sequence using the extended Kalman filter," *IEEE Trans. Biomed. Eng.*, vol. 58, no. 3, pp. 541–549, Mar. 2011.
- [15] V. Barbaro, P. Bartolini, G. Calcagnini, F. Censi, and A. Michelucci, "Measure of synchronisation of right atrial depolarisation wavefronts during atrial fibrillation," *Med. Biol. Eng. Comput.*, vol. 40, pp. 56–62, 2002.
- [16] U. Richter, A. Bollmann, D. Husser, and M. Stridh, "Right atrial organization and wavefront analysis in atrial fibrillation," *Med. Biol. Eng. Comput.*, vol. 47, no. 12, pp. 1237–1246, 2009.
- [17] C. Schilling, M. Nguyen, A. Luiik, C. Schmitt, and O. Dössel, "Non-linear energy operator for the analysis of intracardiac electrograms," in *Proc. World Congress on Medical Physics and Biomedical Engineering 2010*, pp. 872–875.
- [18] R. Houben, N. de Groot, and M. Allesie, "Analysis of fractionated atrial fibrillation electrograms by wavelet decomposition," *IEEE Trans. Biomed. Eng.*, vol. 57, no. 6, pp. 1388–1398, 2010.
- [19] A. Alcaine, F. Simón, A. Arenal, P. Laguna, and J. P. Martínez, "A wavelet-based activation detector for bipolar electrogram analysis during atrial fibrillation," in *Proc. Comput. Cardiology*, 2012, pp. 717–720.
- [20] J. Ng, A. H. Kadish, and J. J. Goldberger, "Effect of electrogram characteristics on the relationship of dominant frequency to atrial activation rate in atrial fibrillation," *Heart Rhythm*, vol. 3, no. 11, pp. 1295–1305, 2006.
- [21] G. Fischer, M. Stuhlinger, C.-N. Nowak, L. Wieser, B. Tilg, and F. Hintringer, "On computing dominant frequency from bipolar intracardiac electrograms," *IEEE Trans. Biomed. Eng.*, vol. 54, no. 1, pp. 165–169, 2007.
- [22] G. W. Botteron and J. M. Smith, "A technique for measurement of the extent of spatial organization of atrial activation during atrial fibrillation in the intact human heart," *IEEE Trans. Biomed. Eng.*, vol. 42, no. 6, pp. 579–586, 1995.
- [23] L. Faes, G. Nollo, R. Antolini, F. Gaita, and F. Ravelli, "A method for quantifying atrial fibrillation organization based on wave-morphology similarity," *IEEE Trans. Biomed. Eng.*, vol. 49, no. 12, pp. 1504–1513, 2002.
- [24] R. Alcaraz and J. J. Rieta, "Review: Application of non-linear methods in the study of atrial fibrillation organization," *J. Med. Biological Eng.*, vol. 33, no. 3, pp. 239–252, 2013.
- [25] P. Sanders, O. Berenfeld, M. Hocini, P. Jaïs, R. Vaidyanathan, L.-F. Hsu, S. Garrigue, Y. Takahashi, M. Rotter, F. Sacher, C. Scavée, R. Ploutz-Snyder, J. Jalife, and M. Haïssaguerre, "Spectral analysis identifies sites of high-frequency activity maintaining atrial fibrillation in humans," *Circulation*, vol. 112, no. 6, pp. 789–797, 2005.
- [26] J. L. Salinet, Sr, G. N. Oliveira, F. J. Vanheusden, J. L. D. Comba, G. A. Ng, and F. S. Schlindwein, "Visualizing intracardiac atrial fibrillation electrograms using spectral analysis," *Comput. Sci. Eng.*, vol. 15, no. 2, pp. 79–87, 2013.
- [27] J. P. Martínez, R. Almeida, S. Olmos, A. P. Rocha, and P. Laguna, "A wavelet-based ECG delineator: Evaluation on standard databases," *IEEE Trans. Biomed. Eng.*, vol. 51, no. 4, pp. 570–581, Apr. 2004.
- [28] T. Oesterlein, M. Keller, S. Schuler, A. Luiik, M. Krüger, G. Seemann, G. Seemann, C. Schmitt, and O. Dössel, "Determination of local activation time in bipolar endocardial electrograms: A comparison of clinical criteria and a new method based on the non-linear energy operator," *J. Electrocardiol.*, vol. 46, no. 4, Paper e18, 2013.
- [29] M. E. Haddad, R. Houben, R. Stroobandt, F. V. Heuverswyn, R. Tavernier, and M. Duytschaever, "Algorithmic detection of the beginning and end of bipolar electrograms: Implications for novel methods to assess local activation time during atrial tachycardia," *Biomed. Signal Process. Control*, vol. 8, no. 6, pp. 981–991, 2013.
- [30] A. Alcaine, D. Soto-Iglesias, D. Andreu, J. Fernández-Armenta, A. Berruezo, P. Laguna, O. Camara, and J. P. Martínez, "Wavelet-based electrogram onset identification for ventricular electroanatomical mapping," in *Proc. Comput. Cardiol.*, 2013, pp. 615–618.
- [31] L. Gepstein, G. Hayam, and S. A. Ben-Haim, "A novel method for nonfluoroscopic catheter-based electroanatomical mapping of the heart: *In vitro* and *in vivo* accuracy results," *Circulation*, vol. 95, no. 6, pp. 1611–1622, 1997.
- [32] J. L. Wells, R. B. Karp, N. T. Kouchoukos, W. A. Maclean, T. N. James, and A. L. Waldo, "Characterization of atrial fibrillation in man: Studies following open heart surgery*," *Pacing Clin. Electrophysiol.*, vol. 1, no. 4, pp. 426–438, 1978.
- [33] K. T. Konings, J. L. Smeets, O. C. Penn, H. J. Wellens, and M. A. Allesie, "Configuration of unipolar atrial electrograms during electrically induced atrial fibrillation in humans," *Circulation*, vol. 95, no. 5, pp. 1231–1241, 1997.
- [34] J. G. Proakis, *Digital Communications*. 4th ed. Englewood Cliffs, NJ, USA: Prentice-Hall, 2001.
- [35] S. Mallat, *A Wavelet Tour of Signal Processing*. New York, NY, USA: Academic, 1999.
- [36] S. Mallat and S. Zhong, "Characterization of signals from multiscale edge," *IEEE Trans. Pattern Anal. Mach. Intell.*, vol. 14, pp. 710–732, 1992.
- [37] A. Cohen and J. Kovačević, "Wavelets: The mathematical background," *Proc. IEEE*, vol. 84, pp. 514–522, 1996.
- [38] P. Laguna, R. Jané, and P. Caminal, "Automatic detection of wave boundaries in multilead ECG signals: Validation with the CSE database," *Comput. Biomed. Res.*, vol. 27, no. 1, pp. 45–60, 1994.
- [39] C. Li, C. Zheng, and C. Tai, "Detection of ECG characteristic points using wavelet transforms," *IEEE Trans. Biomed. Eng.*, vol. 42, no. 1, pp. 21–28, 1995.
- [40] L. Lin, A. S. Hedayat, B. Sinha, and M. Yang, "Statistical methods in assessing agreement: Models, issues and tools," *J. Am. Statist. Assoc.*, vol. 97, no. 457, pp. 257–270, 2002.
- [41] J. Fernández-Armenta, A. Berruezo, D. Andreu, O. Camara, E. Silva, L. Serra, V. Barbarito, L. Carotenutto, R. Evertz, J. T. Ortiz-Pérez, T. M. De Caralt, R. J. Perea, M. Sitges, L. Mont, A. Frangi, and J. Brugada, "Three-dimensional architecture of scar and conducting channels based on high resolution ce-cmr: Insights for ventricular tachycardia ablation," *Circulation: Arrhythmia Electrophysiol.*, vol. 6, no. 3, pp. 528–537, 2013.